Numerical simulation of mixing by Rayleigh–Taylor and Richtmyer–Meshkov instabilities

By D.L. YOUNGS

Atomic Weapons Establishment, Aldermaston, Reading,
Berkshire, RG7 4PR, United Kingdom

Rayleigh–Taylor (RT) and Richtmyer–Meshkov (RM) instabilities at the pusher–fuel interface in inertial confinement fusion (ICF) targets may significantly degrade thermonuclear burn. Present-day supercomputers may be used to understand the fundamental instability mechanisms and to model the effect of the ensuing mixing on the performance of the ICF target. Direct three-dimensional numerical simulation is used to investigate turbulent mixing due to RT and RM instability in simple situations. A two-dimensional turbulence model is used to assess the effect of small-scale turbulent mixing in the axisymmetric implosion of an idealized ICF target.

---

1. Introduction

A typical inertial confinement fusion (ICF) target consists of a dense shell (pusher) filled with DT gas. The shell is imploded by irradiation with laser beams or by other means. Rayleigh–Taylor (RT) instability may occur whenever the pressure gradient opposes the density gradient (i.e., $\nabla p \cdot \nabla \rho < 0$). This situation arises at the ablation front at the outside of the pusher during the shell acceleration phase. The effect of mass ablation plays an important role in reducing instability growth in this case; see for example, Gardner *et al.* (1991). Direct numerical simulation is an ideal way of investigating these effects. However, this is not the subject of the present paper. RT instability also occurs at the pusher–fuel interface toward the end of the implosion phase when the shell is decelerated by the less dense gas. Richtmyer–Meshkov (RM) instability will occur when shocks pass through the pusher–fuel interface. The instabilities occurring in this phase are discussed in the present paper. Implosion asymmetry due to nonuniform irradiation of the target will seed long-wavelength RT and RM instabilities. The surface roughness of the shell will initiate small-scale instability growth over the whole of the pusher–fuel surface, and the resulting turbulent mixing will degrade the performance of the ICF target by reducing the heating of the gas during the implosion phase and by inhibiting the thermonuclear reaction after ignition. The difficulty in modeling the effect of these instabilities on target performance is one of the major uncertainties in calculating target behavior. The aim of this paper is to show that present-day supercomputers may be used both to understand the fundamental mixing processes and to model the effects of these instabilities on the performance of the ICF target.

Three types of calculation are described in this paper. Section 2 gives a summary of the TURMOIL3D computer program that is used for three-dimensional direct simulation of RT and RM mixing in simple situations. Two examples are studied in detail in Sections 3 and 4. It is impractical to use direct three-dimensional numerical simulation to calculate turbulent mixing in real problems where many complex physical processes need to be modeled. A two-dimensional turbulence model therefore is used to assess the combined effect

of long-wavelength asymmetry plus small-scale turbulent mixing. The turbulence model is described in Section 5. Application of the model to an idealized ICF implosion is discussed in Section 7. The turbulence model uses a number of coefficients that are obtained from experimental data on turbulent mixing. It is now feasible to supplement the experimental data with results from direct three-dimensional simulation. In Section 6 it is shown how direct three-dimensional simulation may be used to help validate the two-dimensional turbulence model.

2. The TURMOIL3D computer program

TURMOIL3D is a simple three-dimensional computer program written for direct simulation of turbulent mixing of two fluids due to RT and RM instabilities. The equations solved are the Euler equations plus an equation for the mass fraction, m_1, of fluid 1:

$$\frac{\partial}{\partial t}(\rho m_1) + \mathrm{div}(\rho m_1 \mathbf{u}) = 0.$$

Perfect gas equations of state are used for each fluid. The mixture is assumed to be in pressure and temperature equilibrium. If $\gamma_1, \gamma_2, c_{v1}, c_{v2}$ are the adiabatic constants and the specific heats for the two fluids, then the pressure is given by

$$p = (\gamma - 1)\rho e \qquad \text{where } \gamma = \frac{\gamma_1 m_1 c_{v1} + \gamma_2 m_2 c_{v2}}{m_1 c_{v1} + m_2 c_{v2}}.$$

The Eulerian finite volume numerical method is an extension to three dimensions of the explicit compressible technique of Youngs (1982). A staggered Cartesian grid is used, with mass fraction (m_1), density (ρ), and internal energy (e) defined at cell centers while the velocity components (u,v,w) are defined at cell corners. As in many compressible fluid codes, such as the FLIC method of Gentry *et al.* (1966), the calculation for each time step is divided into two parts, a Lagrangian phase and an advection (or rezoning) phase. In the Lagrangian phase the changes in velocity and internal energy due to pressure terms are calculated, that is, the equations solved are

$$\rho \frac{\partial \mathbf{u}}{\partial \mathbf{t}} = -\nabla \mathbf{p}, \qquad \rho \frac{\partial e}{\partial t} = -p \, \mathrm{div} \, \mathbf{u}.$$

A second-order-accurate time-integration technique is used, and the sum of the kinetic + internal energies is conserved exactly. All three spatial directions are computed simultaneously.

In the advection phase, fluxes across cell sides are calculated. X, Y, and Z advection are calculated in separate steps; the order of calculation is XYZ, ZYX for alternate time steps. Operator splitting facilitates the use of the second-order-accurate, monotonic advection method of van Leer (1977), which is used for all fluid variables ρ, m_1, e, u, v, and w. The aim of the van Leer method is to minimize numerical diffusion while preventing spurious overshoots and undershoots. Many desirable properties follow. For example, the mass fraction m_1 remains in the interval [0,1]. For the mixing of two effectively incompressible fluids the mixture density ρ remains in the interval $[\rho_1, \rho_2]$, thereby avoiding any spurious buoyancy generated turbulence.

The advection phase conserves the masses of each fluid, the internal energy, and the momentum. Kinetic energy tends to be dissipated. The formula due to DeBar (1974) is used to calculate the energy dissipated in each cell. This is added on to the internal energy. Use

of the second-order-accurate van Leer method for momentum advection gives significantly less dissipation than a first-order (upwind) method.

In the Lagrangian phase the time step is controlled by the sound speed (c) that is, the time step must satisfy $\Delta t < \min{(\Delta x, \Delta y, \Delta z)}/c$. For the advection phase the time step is controlled by fluid velocities, and the required condition is $\Delta t < \min{(\Delta x/|u|, \Delta y/|v|, \Delta z/|w|)}$. Several of the simpler Lagrange steps may be performed per advection step. This significantly speeds up low Mach number calculations and means that it is feasible to simulate incompressible mixing problems by carrying out calculations at low Mach numbers.

The numerical method of Youngs (1982) used an interface tracking method for multi-fluid flows. For turbulent mixing of miscible fluids a high degree of molecular mixing is known to occur from experimental results. The numerical method needs to include a mechanism for the dissipation of both concentration and velocity fluctuations due to small-scale eddies. Hence interface tracking is inappropriate. In large eddy simulations, such as those of Moin and Kim (1982), a nondissipative numerical technique is used in conjunction with a subgrid eddy viscosity to represent the effect of the unresolved scales. In TURMOIL3D the monotonicity constraints in the van Leer advection scheme provide the required dissipation at high wavenumbers. Hence, an additional subgrid model is unnecessary. Use of a subgrid model may give a better representation of the high-wavenumber ends of the energy and concentration fluctuation spectra (the $k^{-5/3}$ Kolmogorov law). However, the monotonic advection scheme has a number of advantages as already noted.

The calculations described in this paper were carried out on the CRAY-YMP at Aldermaston. The explicit numerical technique ideally is suited to parallel computing and makes full use of the multitasking capability of the CRAY computers.

3. Three-dimensional simulation of Rayleigh–Taylor mixing

The simplest situation in which RT instability occurs consists of fluid with density ρ_1 resting initially above fluid with density $\rho_2 < \rho_1$ in a gravitational field g. If the plane interface is perturbed, "bubbles" of the less dense fluid 2 rise and "spikes" of the denser fluid 1 fall.

There have been many two-dimensional calculations of this phenomenon. Early results were published by Harlow and Welch (1966) and Daly (1967). More recent calculations are described by Youngs (1984), Tryggvason (1988), Kerr (1988), and Mulder *et al.* (1992). A number of articles have been published by Glimm and his co-workers (Chern *et al.* 1986; Glimm *et al.* 1990); these papers used an interface tracking method and focused on the increase in the length scale associated with the mixing zone, due to interactions between the bubbles of the light fluid. Few simulations of RT instability in three dimensions have been published. The growth of the instability from a single-wavelength initial perturbation has been considered by Dahlburg and Gardner (1990), Tryggvason and Unverdi (1990), and Town and Bell (1991). Three-dimensional calculations of turbulent mixing by RT instability have been performed by Youngs (1991).

In this section, three-dimensional simulation is used to investigate in detail the case when the instability evolves from small random perturbations and when viscosity is negligible. Loss of memory of the initial conditions tends to occur as the dominant length scale associated with the turbulent mixing zone increases with time. Dimensional reasoning then suggests [see Belen'kii and Fradkin (1965), Anuchina *et al.* (1978), and Youngs (1984)] that the mixing zone should be described by a similarity solution with a length scale proportional to gt^2. The width of the mixing zone is then given by

$$\delta = f(\rho_1/\rho_2)\, gt^2. \tag{1}$$

The experiments of Read (1984) and Youngs (1989), in which no deliberately imposed initial perturbations were present, appeared to confirm equation (1). The depth to which the mixing zone penetrated the denser fluid 1 (bubble penetration) was found to be given by

$$h_1 = \alpha \frac{\rho_1 - \rho_2}{\rho_1 + \rho_2} gt^2 = \alpha A gt^2, \qquad (2)$$

where α was approximately 0.06 at all density ratios. If h_2 denotes the depth to which the mixing zone penetrates fluid 2 (spike penetration), then h_2/h_1 was shown to be a slowly increasing function of the density ratio ρ_1/ρ_2. Similar values of α were reported by Kucherenko *et al.* (1991). Andrews and Spalding (1990) gave $\alpha = 0.04$ for a slim two-dimensional tank. Most other experimental estimates of α are higher. The two-dimensional multimode simulations of Youngs (1984,1989) gave $\alpha \sim 0.04$ to 0.05. The three-dimensional simulations described by Youngs (1991) indicated $\alpha = 0.035$ to 0.04, that is, the computed values of α are less than the observed values. In this section, a three-dimensional calculation with improved mesh resolution is described. The aim is to see if this discrepancy persists.

The three-dimensional calculations described here use $270 \times 160 \times 160$ meshes. The computational region is: $-0.65 < x < 0.9$, $0 < y,z < 0.8$. Periodic boundary conditions were used in the y- and z-directions. At the x-boundaries the normal velocity was set to zero. A uniform mesh (250 zones) was used in the interval $-0.5 < x < 0.75$. Extra coarse meshes were added at $x < -0.5$ and $x > 0.75$ to reduce the effect of the boundaries on the growth of the mixing zone. For comparison, results also are shown for two-dimensional calculations with twice the resolution, that is, 540×320 zones. The initial distribution of fluid 1 was given by

$$m_1 = \begin{cases} 1 & x < \zeta_R \\ 0 & x > \zeta_R, \end{cases}$$

where the random interface perturbation ζ_R was a combination of Fourier modes:

$$\zeta_R(y,z) = \mathrm{Re} \sum_{k_{\min} < k < k_{\max}} a_0 \exp(ik_y y + ik_2 z),$$

where

$$k = \sqrt{k_y^2 + k_z^2} = \frac{2\pi}{\lambda}. \qquad (3)$$

The wavenumber range $(k_{\min}, k_{\max})$ corresponded to wavelengths $\lambda = 4\Delta x$ to $8\Delta x$. The random amplitudes a_0 were chosen from a unit Gaussian distribution and then scaled so that the standard deviation of the perturbation was $(\overline{\zeta_R^2})^{1/2} = 0.02\lambda_{\min} = 0.0004$. At the interface the fluid densities were $\rho_1 = 3$ and $\rho_2 = 1$. Before the perturbation was applied, an adiabatic variation was used throughout each fluid, that is, $\partial p/\partial x = \rho g$, $p = a$ constant $\times$ ρ^γ. This gave neutral stability within each fluid and so minimized the effect of compressibility. The initial interface pressure was chosen to be high enough to make compressibility effects negligible. When the interface was perturbed, the pressure distribution was modified (while leaving the density distribution unaltered) to satisfy the Poisson equation

$$\nabla\left(\frac{1}{\rho}\nabla p\right) = 0; \qquad \frac{\partial p}{\partial x} = \rho g \text{ at the } x\text{-boundaries.}$$

This ensured $\partial/\partial t\,(\mathrm{div}\,\mathbf{u}) = 0$ at the perturbed interface. The modification to the pressure distribution is small for the present problem. However, it is more important for the problem considered in Section 6, where a large additional perturbation is added.

Two three-dimensional and four two-dimensional calculations were carried out, with different choices for the random amplitudes a_0. For the purpose of analyzing the results it has proved useful to use volume fractions rather than mass fractions. The volume fraction of fluid i (f_i) is calculated from the mass fractions:

$$f_i = (m_i/\rho_i)/(m_1/\rho_1 + m_2/\rho_2).$$

Figure 1 shows iso-surfaces for $f_1 = 0.99$ from one of the three-dimensional calculations. This shows the evolution of the bubbles of light fluid. The increase with time of the characteristic bubble size is clearly shown. The rate of growth of the mixing zone is measured in two different ways. Bubble and spike penetrations, h_1 and h_2, are defined as the distances from the initial interface position ($x = 0$) to the points where $\bar{f}_1 = 0.99$ and $\bar{f}_1 = 0.01$, respectively. The bar denotes the average over a plane layer, that is:

$$\bar{\phi}(x,t) = \int \phi(x,y,z,t)\,dy\,dz \bigg/ \int dy\,dz.$$

The integral width, used by Andrews and Spalding (1990), is taken to be

$$W = \int \bar{f}_1 \cdot \bar{f}_2\,dx,$$

which is less susceptible to statistical fluctuations. If $\bar{f}_1$ varies linearly with x for 1 to 0, then $h_1 = h_2 = 3W$, that is, the width of the mixing zone is of the order of $6W$.

Figure 2 shows plots of W versus Agt^2 and figure 3 shows plots of h_1 versus Agt^2. For the two-dimensional calculations the plots of W versus Agt^2 show reasonably good linear correlation. However, for the three-dimensional case the initial slope is about twice the value at the end of the calculation. The slope of the curve begins to decrease when the mixing zone exceeds a width of about 50 meshes. It is suggested that the initially high slope is due to the inability to resolve an inertial range during the early stages of the calculation. The reduced slope at the end of the calculation is attributed to the dissipative effect of three-dimensional turbulence on density and velocity fluctuations. The estimated values for the growth rate coefficients are $\alpha \sim 0.03$ in three dimensions and $\alpha \sim 0.04$ in two dimensions.

As in Youngs (1991), the molecular mixing fraction at a given value of x is defined as

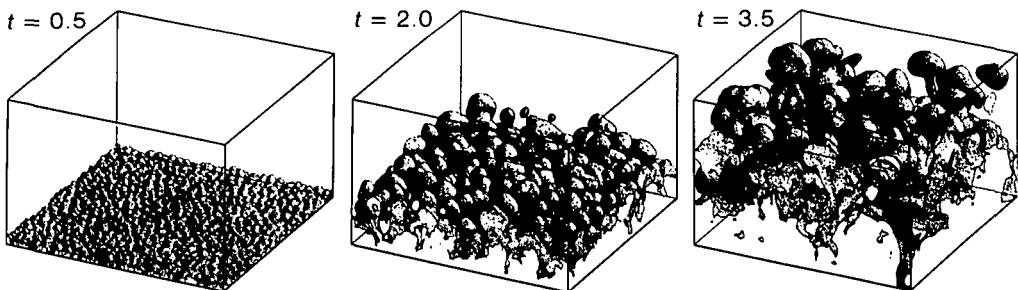$$\theta(x) = \overline{f_1 f_2}/(\bar{f}_1 \cdot \bar{f}_2),$$

FIGURE 1. Iso-surfaces of $f_1 = 0.99$ for the three-dimensional Rayleigh–Taylor calculation in the region $x < 0$. Gravity acts vertically downward.
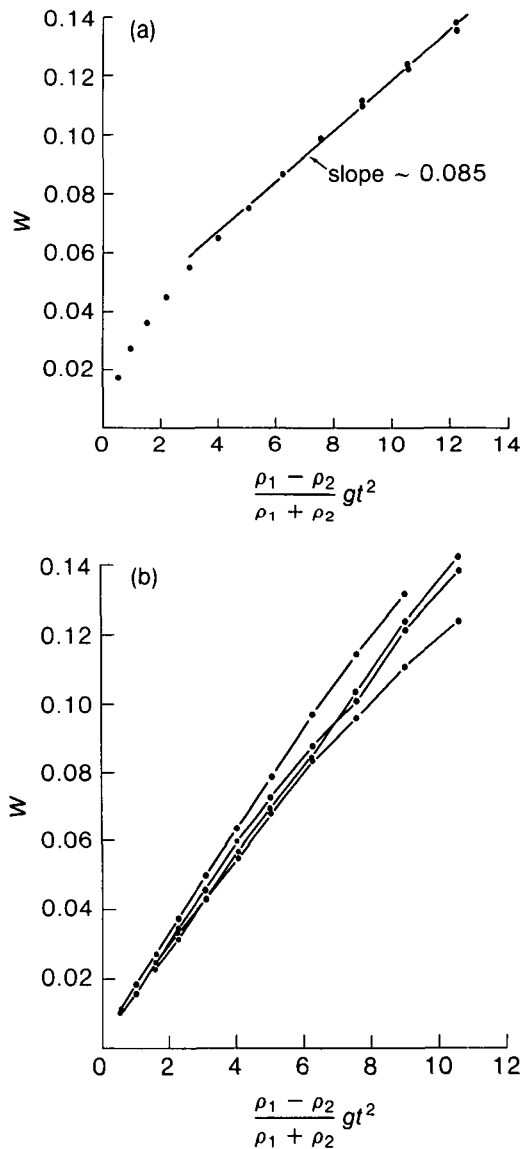
FIGURE 2. Variation of the integral mixing zone width (W) with time for the Rayleigh–Taylor calculations: (a) three dimensions, (b) two dimensions.

and the molecular mixing fraction for the mixing zone as a whole is taken to be

$$\Theta - \int \overline{f_1 f_2}\, dx \Big/ \int \bar{f}_1 \cdot \bar{f}_2\, dx.$$

The overbars denote plane averages, as has been previously explained. If there are no concentration fluctuations at a given value of x, that is, $f_r = \bar{f}_r$, then $\theta(x)$ and Θ are both equal to unity (complete molecular mixing).

If the mixing zone is described by a similarity solution with gt^2 as the only length scale, then Θ should have a constant value (for a given density ratio). Moreover, the x, y, and
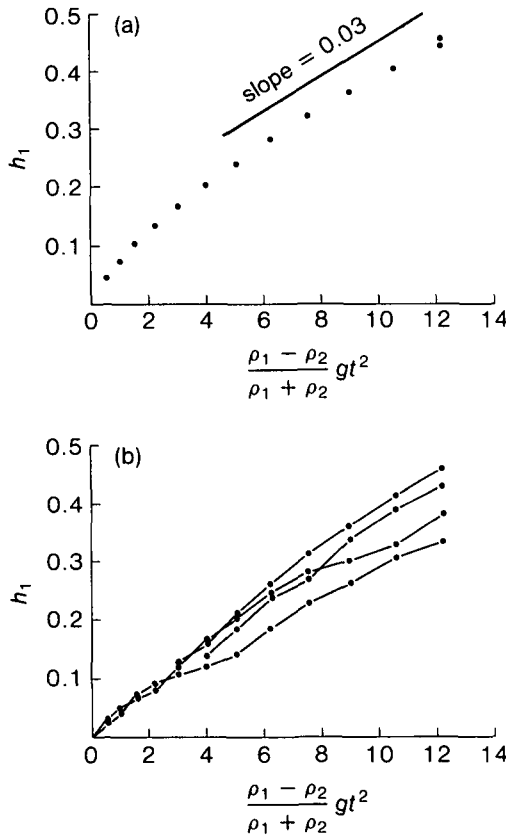
FIGURE 3. Variation of the bubble penetration (h_1) with time for the Rayleigh–Taylor calculations: (a) three dimensions, (b) two dimensions.

z contributions to the kinetic energy (integrated over the mixing zone), $K_x = \frac{1}{2}\int \rho u^2 \, dV$, etc., and the kinetic energy dissipation D should be constant fractions of the total potential energy loss $P = D + K_x + K_y + K_z$. Figure 4 shows plots of Θ, K_x/P, $\frac{1}{2}(K_y + K_z)/P$, and D/P versus $\xi = \Delta x/W$ for the three-dimensional calculations. ξ is a measure of the mesh resolution. The values obtained as $\xi \to 0$ give an indication of the results for the well-resolved similarity solution. The change in the values between $\xi = 0.1$ and $\xi = 0.05$ is not large, indicating that approximate self-similarity is obtained. The limiting values as $\xi \to 0$ are, approximately,

$$\Theta = 0.83$$

$$K_x/P = 0.28$$

$$K_y/P = K_z/P = 0.10$$

$$D/P = 0.52.$$

There is significantly less dissipation in the two-dimensional simulations. At the end of the calculations the molecular mixing fraction is $\Theta \sim 0.54$, and the kinetic energy dissipation is very low, $D/P \sim 0.06$.

Figure 5 shows plots of the layer-averaged quantities $\bar{f_1}$ and θ versus x/W at $t = 2$ and
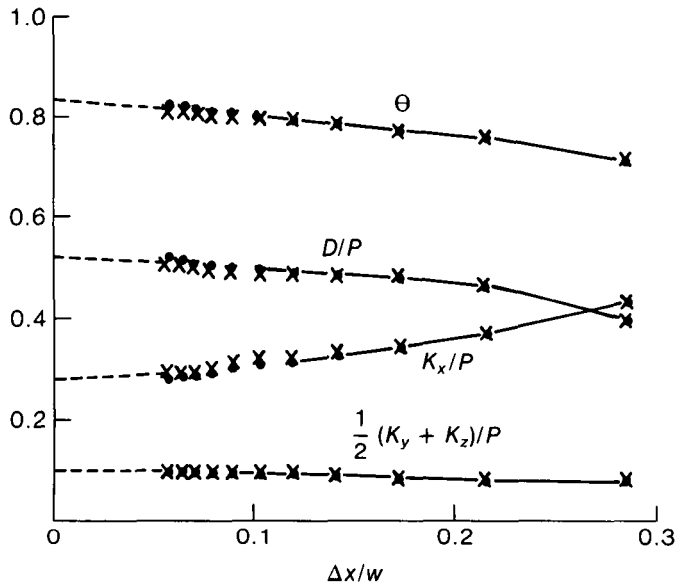
FIGURE 4. Three-dimensional Rayleigh–Taylor calculations: integrated properties of the turbulent mixing zone versus mesh resolution.

$t = 3.5$. The two sets of curves are very similar, again indicating that approximate self-similarity is obtained.

The probability distribution functions (pdf's) for the variable f_1 for the plane layers $x = -2W$, 0 and $2W$ are shown in figure 6 for times $t = 2.0$ and 3.5. Again there is little change between the two times. In the middle of the layer the two fluids are well mixed, that is, there is a low probability of finding $f_1 = 0$ or $f_1 = 1$. The pdf at $x = -2W$ indicates the presence of pure fluid 1 + bubbles of light fluid 2 well mixed with the heavier fluid. Equivalent results apply on the other side of the mixing zone.

All of the results indicate that an approximate self-similar mixing zone is established by the end of the calculation. The final length scale is about eight times larger than the initial length scale; in these circumstances, loss of memory of the initial conditions is expected. However, the calculated value of α is about 0.03, which is significantly less than most of the observed values. A possible explanation is that mixing in the experiments has been enhanced by initial perturbations that are larger than those used in the simulations described here, that is, complete loss of memory of the initial conditions has not occurred.

4. Three-dimensional simulation of Richtmyer–Meshkov mixing

Richtmyer–Meshkov instability occurs when one or more shock waves pass through a perturbed interface or a turbulent mixing zone. The small amplitude theory for a single shock was investigated by Richtmyer (1960); shock tube instability experiments were described by Andronov *et al.* (1976). A simple situation will be considered here: the passage of a single shock wave, at normal incidence, through the planar interface between two fluids with initial densities ρ_1^0 ($x < 0$) and ρ_2^0 ($x > 0$). The results shown here will describe the turbulent mixing that occurs after shock passage. It will be assumed that the initial
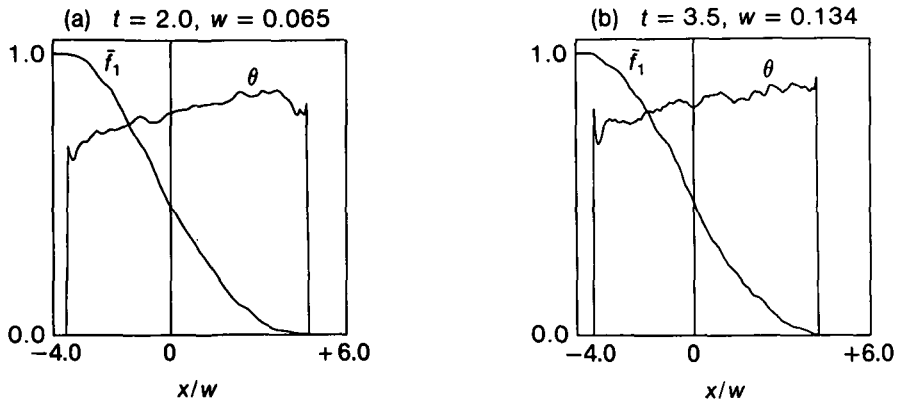
FIGURE 5. Three-dimensional Rayleigh–Taylor calculation. Profiles of layer-averaged fluid 1 volume fraction ($\bar{f}_1$) and molecular mixing fraction (θ).
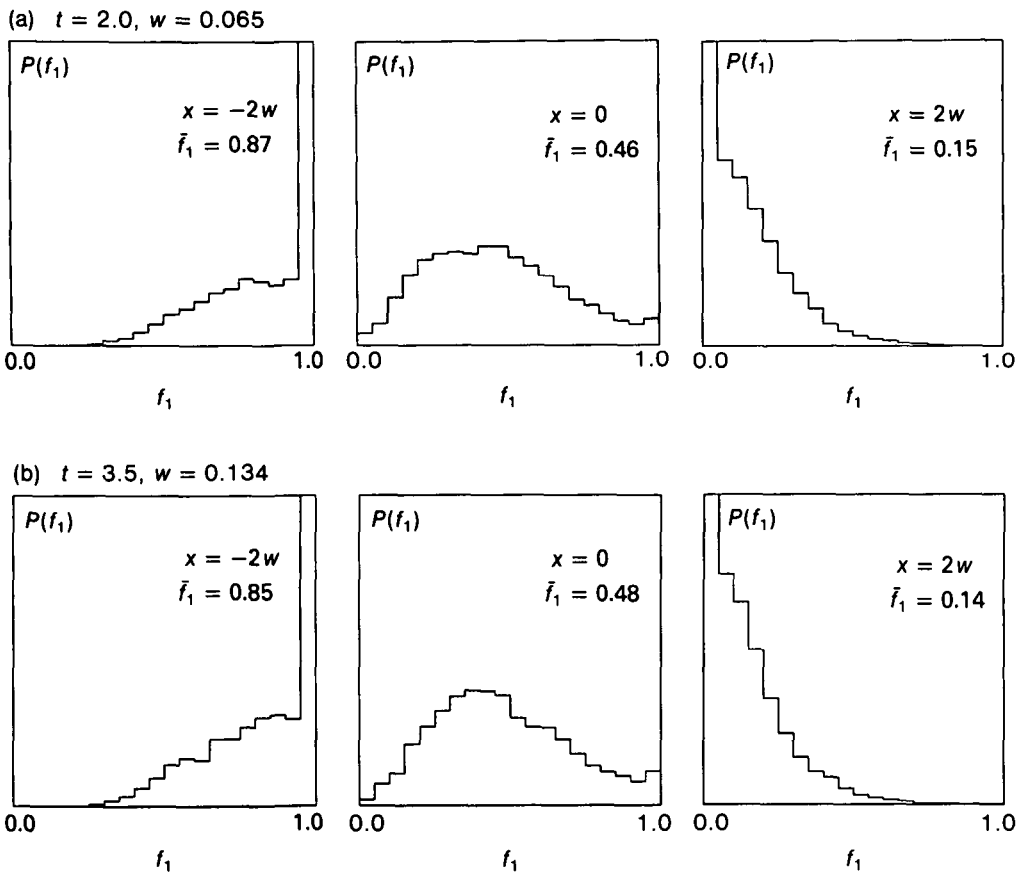

FIGURE 6. Three-dimensional Rayleigh–Taylor calculation. Probability density functions for f_1 in plane layers, $x = $ a constant.

response of the perturbed interface is described by the small amplitude linear theory. For an initial perturbation,

$$\zeta(y) = a_0 \cos ky,$$

the velocity perturbation induced by shock passage is given by $\mathbf{u} = -\nabla\phi$, where

$$\phi = \begin{cases} -\phi_0 \cos ky\, e^{+kx} & x < 0 \\ +\phi_0 \cos ky\, e^{-kx} & x > 0 \end{cases}$$

$$\phi_0 = a_0 U \frac{\rho_1 - \rho_2}{\rho_1 + \rho_2},$$

and U is the change in interface velocity due to the shock.

Richtmyer (1960) argued that, if there was significant compression, it was better to use the values of a_0, ρ_1, and ρ_2 after shock transit. Note that velocity fluctuations are generated for both of the cases $\rho_1 > \rho_2$ and $\rho_1 < \rho_2$.

For the problem considered here, the postshock configuration is used for the initial conditions. The values used for the postshock densities are $\rho_1 = 3$ and $\rho_2 = 1$; the pressure is $p = 1$; $\gamma = \frac{5}{3}$ for both fluids. The corresponding preshock values are $\rho_1^0 = 1.375$, $\rho_2^0 = 0.25$, and $p^0 = 0.0$. The change in fluid velocity due to shock passage is $U = 1.74$. In the simulation the mean velocity is set to zero, that is, the numerical mesh moves with the shocked fluid. The interface perturbation, imagined to be present after shock transit, is given by equation (3) with $k_{\min} = 0$.

In order to calculate the postshock conditions, the initial perturbation actually used is the velocity perturbation induced by the shock. This is derived from a vector potential:

$$\mathbf{u} = \text{curl } \mathbf{A},$$

where

$$A_x = 0.0$$

$$A_y = \text{Re} \sum_{k < k_{\max}} \frac{ik_z}{k} \phi_0 \exp\{ik_y y + ik_z z - k|x|\}$$

$$A_z = \text{Re} \sum_{k < k_{\max}} \frac{ik_y}{k} \phi_0 \exp\{ik_y y + ik_z z - k|x|\}$$

and

$$\phi_0 = \text{amplitude of the scalar potential}$$

$$= a_0 \cdot \frac{\rho_1 - \rho_2}{\rho_1 + \rho_2} \cdot U. \tag{4}$$

The vector potential is calculated at the cell centers. Differentiation then is used to calculate the velocity at the cell corners. For a uniform mesh this gives a divergence-free initial velocity field.

The random initial amplitudes a_0 are chosen from a Gaussian distribution. This gives a flat spectrum in the region $k < k_{\max}$, that is, the standard deviation of the amplitude spectrum is given by

$$\sigma^2 \sim \int dk_y\, dk_z = C \int_0^{k_{\max}} k\, dk,$$

where C is a constant.

For a single mode with amplitude a_0, $\sigma^2 = \frac{1}{2}a_0^2$ and the initial kinetic energy per unit interfacial area obtained by integration of the velocity distribution given by equation (4) is

$$\frac{1}{2}(\rho_1 + \rho_2)k\sigma^2 \left(\frac{\rho_1 - \rho_2}{\rho_1 + \rho_2}\right)^2 U^2.$$

Hence, for the random initial amplitude the initial kinetic energy is

$$K_0 = \frac{1}{2}(\rho_1 + \rho_2)\left(\frac{\rho_1 - \rho_2}{\rho_1 + \rho_2}\right)^2 U^2 C \int_0^{k_{max}} k^2 \, dk$$

$$= \frac{1}{3}(\rho_1 + \rho_2)k_{max}\sigma^2 \left(\frac{\rho_1 - \rho_2}{\rho_1 + \rho_2}\right)^2 U^2.$$

As for the Rayleigh–Taylor calculations described in the previous section, W is used to denote the integral width of the mixing zone, $\int \bar{f}_1 \bar{f}_2 \, dx$. The x-component of the initial velocity at the interface u_0 has a Gaussian distribution. It may therefore be shown that

$$V_0 = \left(\frac{dW}{dt}\right)_{t=0} = c\langle u_0^2 \rangle^{1/2},$$

where

$$c = \frac{1}{\sqrt{2}} \int_0^\infty [1 - erf^2(s)] \, ds = 0.564$$

and

$$\langle u_0^2 \rangle^{1/2} = \frac{1}{\sqrt{2}} k_{max}\sigma U \left|\frac{\rho_1 - \rho_2}{\rho_1 + \rho_2}\right|. \tag{5}$$

Most of the initial kinetic energy corresponds to wavenumbers near k_{max}, that is, the initial length scale is of the order of λ_{min}. The initial growth of the perturbation is described by the linear theory. However, when the width of the mixing zone is of the order λ_{min}, a turbulent layer will develop. The late-time behavior of this turbulent layer was investigated by Barenblatt (1983) and Neuvazhayev (1991). By considering self-similar solutions to turbulent diffusion equations, it was shown that at late time the mixing zone width should vary as t^p, where p is less than unity. A simple argument may be used to demonstrate this behavior. Suppose that the velocity field is characterized by a length scale L and a magnitude V. L increases as the mixing zone grows; the initial value is determined by λ_{min}. The turbulence kinetic energy is dissipated by the cascade to high wavenumbers (the Kolmogorov process) at the rate V^3/L per unit mass. This suggests the following model equations:
kinetic energy dissipation,

$$\frac{d}{dt}(LV^2) = -aV^3;$$

increase in mixing zone width,

$$\frac{dW}{dt} = V;$$

length scale,

$$L = bW + c\lambda_{min}.$$

a, b, c are model constants. The initial values are $W = 0$, $V = V_0$. The solution for W is

$$\frac{W}{\lambda_{min}} = A\left\{ \left(1 + \frac{V_0 t}{pA\lambda_{min}}\right)^p - 1 \right\}, \tag{6}$$

where

$$A = \frac{c}{b}$$

and

$$p = \frac{2}{3 + ab}.$$

If there were no kinetic energy dissipation (i.e., $a = 0$), p would be $\frac{2}{3}$. For nonzero dissipation, $p < \frac{2}{3}$.

Two-dimensional numerical simulations of RM instability have been described by Mikaelian (1991), Cloutman and Wehner (1992), and Pham and Meiron (1993). For multiple-scale random perturbations, Pham and Meiron (1993) give some evidence of t^p behavior at late time. As for RT instability, little has been published on three-dimensional simulation; Cloutman and Wehner (1992) showed results for single-mode calculations.

Results are presented here for two- and three-dimensional calculations. The three-dimensional calculation used $270 \times 160 \times 160$ zones, the same number as for the Rayleigh–Taylor mixing layer. The interface position was, however, changed as h_2/h_1 was greater in this case; in the x-direction the computational region was $0.55 < x < 1.0$. The minimum wavelength for the initial perturbation was $\lambda_{min} = 16\,\Delta y$, that is, the initial scale was well resolved. The two-dimensional calculation used 540×320 zones and also had $\lambda_{min} = 16\,\Delta y$. In order to be as consistent as possible with the three-dimensional calculation, a $k_y\,dk_y$ spectrum was used for the random initial amplitudes, giving

$$\sigma^2 = C\int_0^{k_{max}} k_y\,dk_y = C\int_0^{k_{max}} k\,dk,$$

as in the three-dimensional case. For both the two- and three-dimensional cases, the random initial amplitudes were scaled in order to satisfy equation (5) exactly. Both calculations then had the some value or V_0.

The simple model considered earlier in this section suggests plotting W/λ_{min} versus $V_0 t/\lambda_{min}$. This is shown in figure 7. The comparison of the two- and three-dimensional results shows some interesting features. Initially, dW/dt is the same for the two calculations, as expected. In the early nonlinear phase, mixing is more rapid in three dimension than in two. However, at late time, when the turbulence is fully developed, the growth rate is less in the three-dimensional simulation. The latter is to be expected since the three-dimensional turbulence is more dissipative than the two-dimensional turbulence. Properties of the turbulent mixing layer at late time ($V_0 t/\lambda_{min} = 50$) are given in table 1. The values of final/initial kinetic energy, K/K_0, clearly show that dissipation of kinetic energy is much greater in three dimensions. The factor 10 difference in kinetic energy between the two- and three-dimensional calculations suggests a factor $\sqrt{10}$ in the growth rate $\dot{W}$. The difference in the growth rates (figure 7) is not as marked as this and implies that the proportionality between $\dot{W}$ and $\sqrt{K/W}$ is different in two and three dimensions.

Equation (6) has been fitted to the three-dimensional data shown in figure 7. The fit is reasonably good but not perfect. Hence, to obtain the best estimate of p ($W \sim t^p$ at late time), the data for $V_0 t/\lambda_{min} > 15$ were approximated by the equation $W = B(t - t_0)^p$. This
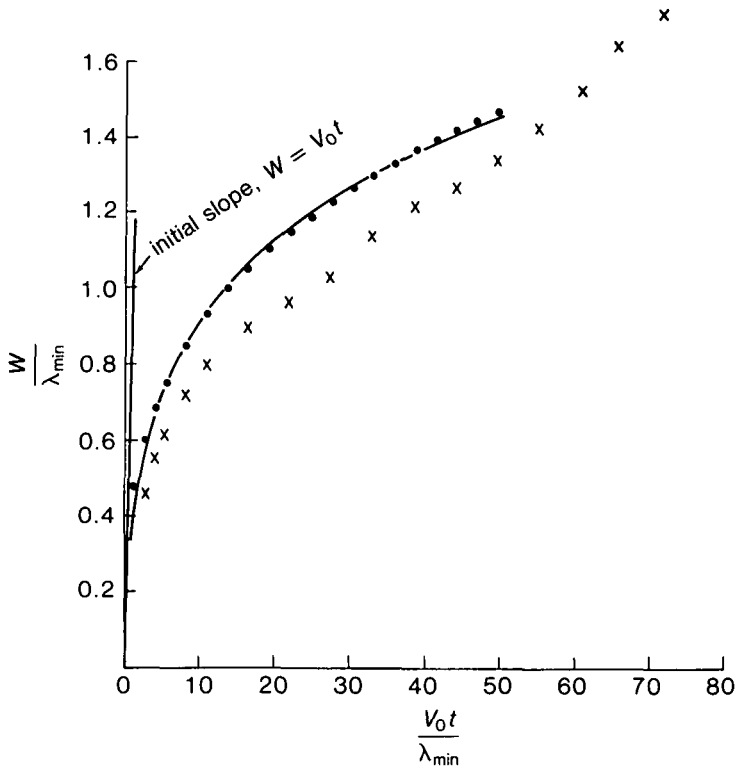
FIGURE 7. Richtmyer–Meshkov calculations. Variation of integral mixing zone width (W) with time: • three dimensions; x two dimensions. The curve drawn is the best fit to the three-dimensional data, using equation (6).

corresponded with the data accurately and gave $p = 0.30$. However, the calculation needs to be run to a much later stage to be certain of the final power law behavior. This is not feasible at present. It should be emphasized that the results shown in figure 7 apply to the case $\rho_1/\rho_2 = 3$ and for the form of the initial perturbation used here. Richtmyer–Meshkov mixing due to a single shock does depend on the initial conditions, and different forms for the initial perturbations are likely to give different values for p.

Figure 8 shows contour plots for the Richtmyer–Meshkov calculations. At the same values of $V_0 t/\lambda_{\min}$ there is more evidence of fine scale mixing in the three-dimensional calculation than in the two-dimensional calculation. In addition, there are some unusual

TABLE 1. Properties of the Richtmyer–Meshkov mixing layer at $V_0 t/\lambda_{\min} = 50$

	Two Dimensions	Three Dimensions
Molecular mixing fraction θ	0.62	0.74
K/K_0	0.46	0.044
K_x/K	0.54	0.57

$$\frac{V_0 t}{\lambda_{min}} = 0.275 \qquad \frac{V_0 t}{\lambda_{min}} = 2.75 \qquad \frac{V_0 t}{\lambda_{min}} = 27.5$$

10 λ_{min}
160 meshes

(a)

$$\frac{V_0 t}{\lambda_{min}} = 0.275 \qquad \frac{V_0 t}{\lambda_{min}} = 2.75 \qquad \frac{V_0 t}{\lambda_{min}} = 27.5 \qquad \frac{V_0 t}{\lambda_{min}} = 82.5$$
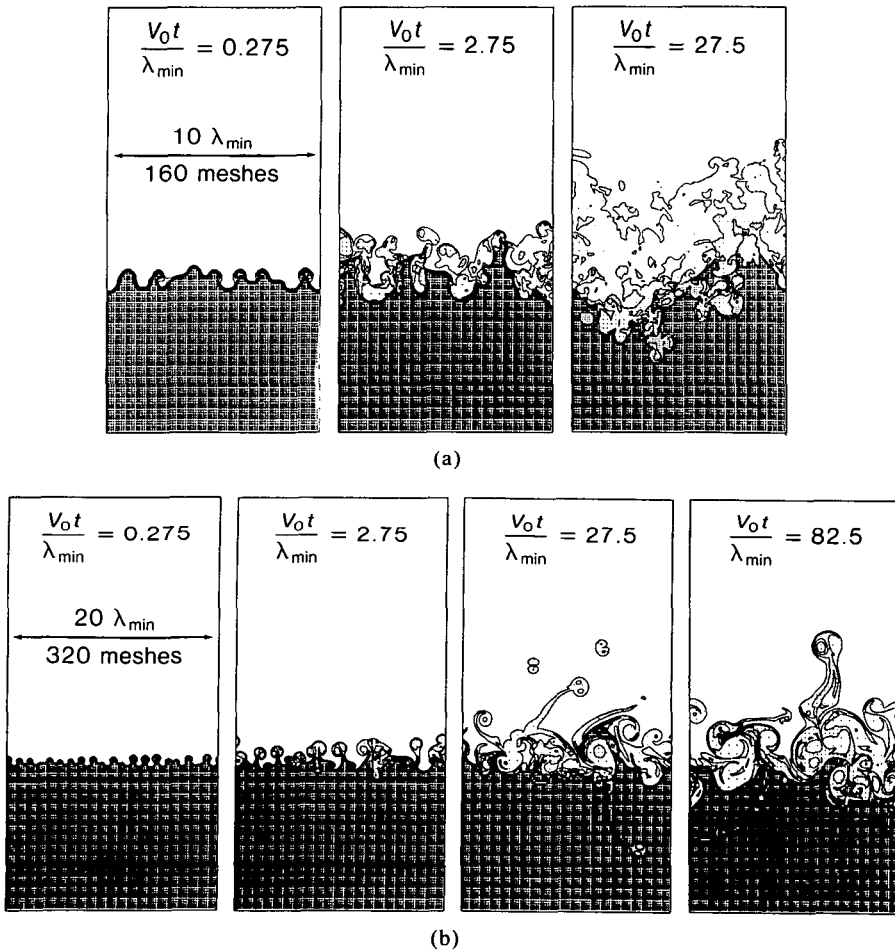
20 λ_{min}
320 meshes

(b)

FIGURE 8. Richtmyer–Meshkov calculations. Volume fraction contours for plane sections, z = a constant. Contour levels $f_1 = 0.05, 0.3, 0.7, 0.95$. (a) Three dimensions, (b) two dimensions.

features in the two-dimensional calculation. The initial velocity field has regions or positive and negative vorticity, and in some parts of the problem this leads to the formation of vortex pairs that propagate away from the mixing zone without being strongly dissipated. The small amounts of fluids carried away from the main part of the mixing zone do not significantly effect the integral mixing zone width W.

There is clearly scope for further application of three-dimensional direct numerical simulation to RM mixing for both the single-shock and the multiple-shock cases (not considered here).

5. The two-dimensional turbulence model

Direct three-dimensional numerical simulation is possible in simple situations such as the cases considered in Sections 3 and 4. However, for more complex real applications, direct three-dimensional simulation is impractical and will probably remain so for many years, in spite of the advances in computer hardware. For such problems it is necessary to use a turbulence model to predict the "average" behavior of the turbulent mixing zone.

For one-dimensional problems in which the mean fluid velocity is normal to the interfaces, RT and RM instabilities are the important processes. One-dimensional turbulence models for such situations have been considered by several authors. Turbulent diffusion models of various levels of complexity have been described by Belen'kii and Fradkin (1965), Neuvazhayev (1975), Andronov *et al.* (1976), Crowley (1992), and Polionov (1991). An alternative approach based on the equations of multiphase flow was considered by Youngs (1984, 1989). The equations of multiphase flow describe the effect of a pressure gradient on fluids of different densities. It is argued here that this represents the RT and RM processes better than a pure diffusion model. However, diffusion models have one advantage: They are significantly easier to implement in a computer code. Use of the equations of a two-phase flow to model mixing by RT instability has also been considered by Andrews (1992), Spalding (1987), and Besnard and Harlow (1988). Besnard *et al.* (1989) described an extended diffusion model that incorporates aspects of the two-phase flow equations.

In some applications, such as the axisymmetric implosion of an ICF target, the mean flow is two dimensional. For such problems a two-dimensional turbulence model is required. This section describes the extension to two dimensions of the model described by Youngs (1989). Turbulent diffusion terms are included in the model. This enables mixing by Kelvin–Helmholtz (KH) instability to be represented in addition to RT and RM mixing.

The two-dimensional version of the multifluid turbulence model has been implemented in a two-dimensional Eulerian hydrocode that uses the method described by Youngs (1982). The equations solved are given in the remainder of this section.

The notation used is as follows:

f_r = fraction by volume of fluid r;
ρ_r = density of fluid r;
$\rho = \Sigma_r f_r \rho_r$, mean fluid density;
$m_r = f_r \rho_r / \rho$, fraction by mass of fluid r;
e_r = internal energy of fluid r;
p_r = pressure of fluid r;
u_{ri} = ith component of the velocity of fluid r (mass weighted);
$\tilde{u}_i = \Sigma m_r u_{ri}$, mass weighted mean velocity;
$\bar{u}_i$ = volume weighted mean velocity;
k = turbulence kinetic energy per unit mass;
L = length scale (average size of bubbles on drops);
g_i = gravitational force per unit mass.

The model equations are then as follows (summation over repeated spatial indices i, j, or k is assumed):

mass transport

$$\frac{\partial}{\partial t}(\rho_r f_r) + \frac{\partial}{\partial x_j}(\rho_r f_r u_{rj}) = 0; \tag{7}$$

momentum transport:

$$\frac{\partial}{\partial t}(\rho_r f_r u_{ri}) + \frac{\partial}{\partial x_j}(\rho_r f_r u_{rj} u_{ri}) = -f_r \frac{\partial p}{\partial x_i} - m_r \frac{\partial R_{ij}}{\partial x_j} + \sum_s (D_{rsi} + M_{rsi}) + \rho_r f_r g_i; \tag{8}$$

internal energy transport

$$\frac{\partial}{\partial t}(\rho_r f_r e_r) + \frac{\partial}{\partial x_j}(\rho_r f_r u_{rj}) = -h_r p_r \frac{\partial \bar{u}_j}{\partial x_j} + \frac{\partial}{\partial x_j}\left(\rho_r f_r D \frac{\partial e_r}{\partial x_j}\right) + \epsilon; \tag{9}$$

turbulence kinetic energy:

$$\frac{\partial}{\partial t}(\rho k) + \frac{\partial}{\partial x_j}(\rho k \tilde{u}_j) = \frac{\partial}{\partial x_j}\left(\rho D_k \frac{\partial k}{\partial x_j}\right) + S_k - \epsilon; \tag{10}$$

length scale:

$$\frac{\partial L}{\partial t} + u_{Lj}\frac{\partial L}{\partial x_j} = \frac{\partial}{\partial x_j}\left(D_L \frac{\partial L}{\partial x_j}\right) + S_L + e_L L. \tag{11}$$

A number of terms in equations (8) to (11) need further explanation. D_{rsi} denotes the drag force on fluid r due to fluid s. This is obtained by extension of the one-dimensional formula described by Youngs (1989):

$$D_{rsi} = -c_1 \frac{\rho_{rs} f_r f_s}{L} W(u_{ri} - u_{si} - w_{ri} + w_{si}),$$

where

$$\rho_{rs} = (f_r \rho_r + f_s \rho_s)/(f_r + f_s),$$

$$W = |\boldsymbol{u}_r - \boldsymbol{u}_s + \boldsymbol{w}_r - \boldsymbol{w}_s|,$$

$$w_{ri} = -\frac{D}{f_r \rho_r}\frac{\partial}{\partial x_i}(f_r \rho_r),$$

D = turbulent diffusion coefficient,

c_1 = drag coefficient.

w_{ri} is the value of $u_{ri} - \bar{u}_i$ expected if mixing is entirely due to turbulent diffusion. For the high drag limit $(c_1 \to \infty)$, $u_{ri} - u_{si} = w_{ri} - w_{si}$. It then follows that $u_{ri} = \bar{u}_i + w_{ri}$ and equation (7) reduces to the diffusion equation

$$\frac{\partial}{\partial t}(\rho_r f_r) + \frac{\partial}{\partial x_j}(\rho_r f_r \bar{u}_j) = \frac{\partial}{\partial x_j}\left\{D\frac{\partial}{\partial x_j}(f_r \rho_r)\right\}.$$

The added mass effect for fluid r due to fluid s is

$$M_{rsi} = -c_a \rho_{rs} f_r f_s \left\{\frac{D_r u_{ri}}{Dt} - \frac{D_s u_{si}}{Dt}\right\},$$

where

$$\frac{D_r u_{ri}}{Dt} = \frac{\partial u_{ri}}{\partial t} + u_{rj}\frac{\partial u_{ri}}{\partial x_j}$$

is the acceleration of fluid r. The coefficient c_a is chosen to be 0.5, the value for a solid sphere of fluid r surrounded by fluid s.

The components of the Reynolds stress are given by the formula used in the (k, ϵ) turbulence model:

$$R_{ij} = \tfrac{2}{3}\rho k \delta_{ij} - 2\mu_t\{\tilde{e}_{ij} - \tfrac{1}{3}\tilde{e}_{kk}\delta_{ij}\},$$

where

$$\tilde{e}_{ij} = \frac{1}{2}\left\{\frac{\partial \tilde{u}_i}{\partial x_j} + \frac{\partial \tilde{u}_j}{\partial x_i}\right\}$$

is the strain rate tensor based on the mass weighted mean velocity and μ_t is the turbulent viscosity.

Use of mass fraction (m_r) weighting in the Reynolds stress terms in equation (8) was explained by Youngs (1989). This is chosen so that the Reynolds stress terms do not induce velocity separation. The velocity separation induced by turbulent diffusion effects is fully accounted for by the inclusion of w_{ri} in the drag term.

The total work done in compressing the fluid is $-p \operatorname{div} \bar{u}$ where $\bar{u}$ is the volume-weighted velocity (not the mass-weighted mean velocity). This gives the correct behavior for the incompressible limit (i.e., work done = zero) where $\operatorname{div} \bar{u} = 0$ but $\operatorname{div} \tilde{u} \neq 0$. The fluid r velocity, u_{ri}, used in the model equations denotes the mass-weighted velocity of fluid r; the fluid r momentum per unit volume is then $\rho_r f_r u_{ri}$ [as implied by equation (8)].

u_{ri} will differ from the volume-weighted value $\bar{u}_{ri}$, unless ρ_r is constant. It is assumed that the difference between u_{ri} and $\bar{u}_{ri}$ is due entirely to diffusion effects and is given by

$$
u_{ri} - \bar{u}_{ri} = -\frac{D}{\rho_r f_r} \frac{\partial}{\partial x_i} \rho_r f_r + \frac{D}{f_r} \frac{\partial f_r}{\partial x_i} = w_{ri} + \frac{D}{f_r} \frac{\partial f_r}{\partial x_i}.
$$

The volume-weighted mean velocity is then given by

$$
\bar{u}_i = \sum_r f_r \bar{u}_{ri} = \sum_r f_r (u_{ri} - w_{ri}).
$$

In the internal energy equation for fluid r, equation (9), the work done in compressing fluid r is $-h_r p_r \operatorname{div} \bar{u}$. h_r depends on the relative compressibility of fluid r and is given by

$$
h_r = f_r / (\rho_r c_r^2) \Big/ \sum_s f_s / (\rho_s c_s^2).
$$

Energy conservation then requires that the mean pressure is given by $p = \Sigma h_r p_r$. The components of the mixture are not forced to be in pressure equilibrium, that is, $p_r \neq p_s$. Instead, an advection equation is solved for the volume fractions:

$$
\frac{\partial f_r}{\partial t} + \bar{u}_j \frac{\partial f_r}{\partial x_j} + \frac{\partial}{\partial x_j} \{ f_r (\bar{u}_{rj} - \bar{u}_j) \} = 0.0.
$$

Pressure differences are then allowed to relax toward zero. The components of the mixture in a computational mesh that are at high pressure expand and do work on the components at low pressure.

Equation (10) for turbulence kinetic energy is essentially the same as that used in the (k, ϵ) model, see for example, Launder and Spalding (1972). The dissipation term is

$$
\epsilon = 0.09 \rho k^{1/2} / \ell_t,
$$

where ℓ_t is the turbulence length scale. The source term in equation (10) is obtained by considering the loss of kinetic energy implied by equations (7), (8), and (9). The result obtained is

$$
S_k = \sum_{r>s} (u_{si} - u_{ri})(M_{rsi} + D_{rsi}) - R_{ij} \tilde{e}_{ij}.
$$

The advection velocity u_{Li} and the source term S_L in the length scale equation (11) are extensions to higher dimensions of the formulas used by Youngs (1989) and Andrews (1992):

$$u_{Li} = \bar{u}_i + \sum_{r>s} f_r f_s (f_r - f_s)(u_{si} - u_{ri}) \bigg/ \sum_{r>s} f_r f_s$$

$$S_L = \sum_{r>s} f_r f_s \sqrt{s}(u_{sj} - u_{rj}) n_{rsj} \bigg/ \sum_{r>s} f_r f_s,$$

where

$$s = \frac{2\rho_{rs}}{\rho_r + \rho_s}.$$

n_{rsi} is a unit vector in the direction of mixing from fluid r to fluid s. This is assumed to be in the direction of

$$f_r \frac{\partial f_s}{\partial x_i} - f_s \frac{\partial f_r}{\partial x_i}.$$

For the two-fluid case, S_L is proportional to the component of velocity separation normal to the interface. For a planar one-dimensional problem this corresponds to the rate of change of the mixing width δ and hence gives $L \sim \delta$. The multifluid formula is simply a plausible extension of the two-fluid formula.

The term $e_L L$ describes the response of the length scale to the strain rate:

$$e_{ij} = \frac{1}{2}\left(\frac{\partial \bar{u}_i}{\partial x_j} + \frac{\partial \bar{u}_j}{\partial x_i}\right).$$

If there are no velocity gradients, $e_L = 0$. For isotropic compression, with $e_{ij} = e\delta_{ij}$, $e_L = e$ seems the obvious choice, that is, the length scale is compressed at the same rate as the fluid. However, the effect of anisotropic strain is uncertain. Andrews (1992) proposed that fluid stretching should reduce the length scale. The form used here is

$$e_L = \tfrac{1}{3} e_{kk} - c_3 |n_i e_{ij}' n_j|,$$

where

$$e_{ij}' = e_{ij} - \tfrac{1}{3} e_{kk} \delta_{ij},$$

n_i = a unit vector in the direction of mixing (normal to the interface), and c_3 is a model constant.

The turbulent viscosity and turbulent diffusion coefficients are chosen by considering turbulent shear flow experiments. The values used here are

$$\mu_t = \rho k^{1/2} \ell_t$$

$$D = D_k = D_L = 2k^{1/2} \ell_t.$$

Finally, the turbulence length scale is taken to be

$$\ell_t = c_2 L.$$

Three model constants, c_1, c_2, and c_3, remain to be determined. Determination of the coefficient c_3 requires comparison with two-dimensional mixing experiments. A precise value is yet to be determined; however, the results quoted by Andrews (1992) suggest that $c_3 = 1$ is plausible, and this is the value used here.

The value of c_2 that determines the relative importance of the turbulent diffusion terms is found by considering a simple incompressible Kelvin–Helmholtz mixing problem with zero gravity for which pressure-driven mixing is negligible. The initial conditions are

$$\rho = \begin{cases} \rho_1 & y < 0 \\ \rho_2 & y > 0 \end{cases}$$

$$u = \begin{cases} u_1^0 & y < 0 \\ u_2^0 & y > 0 \end{cases}$$

$$v = w = 0.$$

It is assumed that this time-evolving mixing layer is equivalent to the spatially evolving plane mixing layer for which many experimental results are available; see, for example, Brown and Roshko (1974) and Batt (1977). For the time-evolving case the width of the mixing layer is given by

$$\delta = f(\rho_1/\rho_2)|u_1^0 - u_2^0|t.$$

The results of Brown and Roshko (1974) at $\rho_1/\rho_2 = 1$ and 7 are fitted by using

$$c_2 = 0.105 + 0.06 \left| \frac{\rho_1 - \rho_2}{\rho_1 + \rho_2} \right|.$$

The drag coefficient, c_1, has then been adjusted to give $\alpha = 0.05$ for Rayleigh–Taylor mixing at all density ratios. The choice of the value of α is somewhat uncertain, as the experimental estimates are higher than those obtained from the three-dimensional simulation. For the purpose of illustrating the use of the turbulence model an intermediate value has been chosen. The required drag coefficient is

$$c_1 = 20 + 5 \left| \frac{\rho_1 - \rho_2}{\rho_1 + \rho_2} \right|.$$

There is one major omission in the model described here. Dissipation of density fluctuations, which was shown to be significant in Sections 3 and 4, has not been taken into account. It is planned to represent this in future versions of the turbulence model by including mass transfer between the fluids.

6. Comparison of two-dimensional turbulence model with direct three-dimensional simulation

It is impractical to apply three-dimensional simulation to real applications. However, it is feasible to simulate more complex problems than the simple one-dimensional mixing layers considered in Sections 3 and 4. It is possible to investigate the validity of the two-dimensional turbulence model by comparison with three-dimensional direct simulation for simple mixing problems that are on average two dimensional. An example is shown in this section.

The problem considered is a modification of the RT mixing layer considered in Section 3. The only change is the initial perturbation, which is now given by

$$\zeta(y,z) = \zeta_F(y) + \zeta_R(y,z).$$

The random perturbation ζ_R is the same as defined in Section 3. A fixed perturbation ζ_F, which depends on y only, is added. As ζ_R is a stationary random function of y and z, averaging of a fluid property $\phi(x,y,z,t)$ over different choices for the initial conditions yields an ensemble average $\langle \phi \rangle$ that depends only on x, y, and t. The aim of the two-dimensional turbulence model is to predict the ensemble-averaged fluid variables.

The two-dimensional turbulence model cannot be expected to be applicable in all situations. If $\zeta_F(y) = 0$, that is, the problem is one dimensional on average, the turbulence model is chosen to fit the quadratic growth law, equation (2). Hence it is assumed that loss of memory of the initial conditions occurs (approximately, at least). Roughly speaking, this means that the random perturbation $\zeta_R(y, z)$ should not include large-amplitude long-wavelength modes that would give enhanced mixing. For the two-dimensional situation, that is, $\zeta_F(y) \neq 0$, the two-dimensional turbulence model will only be valid if a similar condition holds. It is not claimed here that this condition will necessarily hold in all ICF applications. Whether it does or not is a matter of current debate. If loss of memory of the initial conditions does occur, then the line average

$$\bar{\phi} = \int_{Z_{\min}}^{Z_{\max}} \phi(x, y, z, t)\, dz / (Z_{\max} - Z_{\min})$$

should be approximately equal to the ensemble average $\langle \phi \rangle$. A single three-dimensional calculation will therefore be performed and line averages will be compared with the two-dimensional turbulence model calculation.

The three-dimensional RT calculation with $270 \times 160 \times 160$ meshes described in Section 3 has been repeated with an extra perturbation, $\zeta_F(x)$, a groove with a cylindrical cross section. The width of the groove is 0.16 and its depth is 0.03. The equivalent two-dimensional turbulence model calculation uses 135×80 meshes. The direct simulation has also been run as a two-dimensional problem ($270 \times 160 \times 1$ meshes).

The three-dimensional simulation, figure 9, shows that the cylindrical groove evolves into a large bubble which penetrates much further into the heavier fluid than the turbulent mixing zone. As time proceeds, the bubble entrains more and more of the heavier fluid; the contour plots show that the maximum value of $\bar{f}_2$ within the bubble decreases with time. Figure 10 compares a section $z = a$ constant with results from the two-dimensional simulation. The growth of the bubble is similar in two and three dimensions. However, there is more fine-scale structure in the three-dimensional simulation.

Results from the turbulence model calculation are shown in figure 11. On the whole, the results are very similar to the direct three-dimensional simulation. However, there are some differences; at late time, the bubble has entrained more of the heavier fluid in the direct
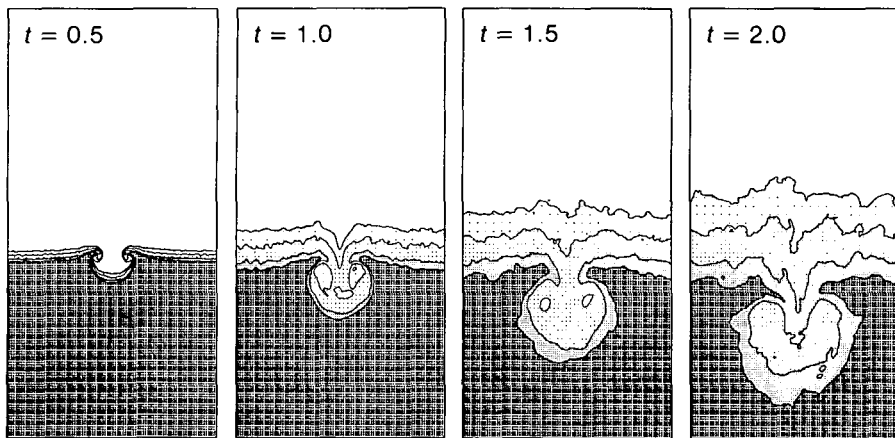

FIGURE 9. Cylindrical groove problem. Three-dimensional simulation. Contours of line averaged volume fraction $\bar{f}_1 = 0.05, 0.3, 0.7, 0.95$.
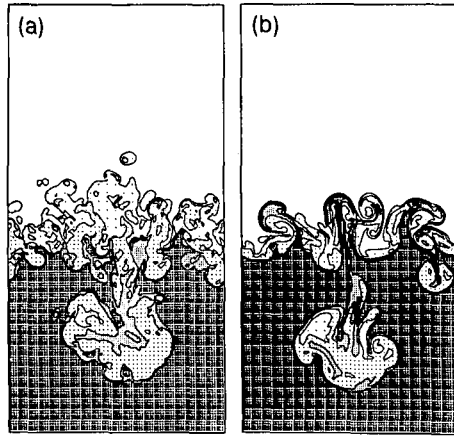
FIGURE 10. Cylindrical groove problem. Comparison of two- and three-dimensional simulations. (a) Three-dimensional volume fraction contours for a plane section $z =$ a constant. (b) Two-dimensional volume fraction contours. Contour levels: $f_1 = 0.05, 0.3, 0.7, 0.95$.

simulation than in the turbulence model calculation. The comparison clearly demonstrates how direct numerical simulation can be used to help to validate two-dimensional turbulence models.

7. Application of the two-dimensional turbulence model to an idealized ICF implosion

An ICF implosion test problem taken from Town and Bell (1991) is used to illustrate the use of the two-dimensional turbulence model. The unperturbed initial spherical geometry that represents a DT/glass ICF capsule at the end of the shell acceleration phase is shown in table 2. Realistic equations of state are used. A simple model is used for the thermal flux, $\mathbf{F} = -k\nabla T$, where k allows for both electron conduction and photon diffusion. Thermal
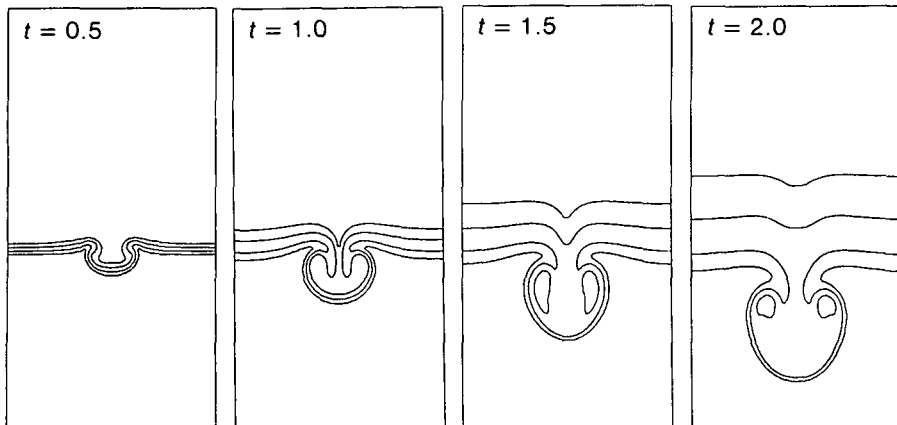

FIGURE 11. Cylindrical groove problem. Two-dimensional turbulence model calculation. Volume fraction contours $f_1 = 0.05, 0.3, 0.7, 0.95$.

TABLE 2. Initial geometry used for the implosion calculations

Material	DT Gas	Glass Shell	Ablated Glass
Density (g/cc)	0.5	5	0.5
Outer radius (μm)	130	190	300
Pressure (Mb)	20	20	20
Inward velocity (cm/μs)	0	15	15

smoothing reduces the density ratio at the gas/shell interface from $\rho_1/\rho_2 \sim 10$ to $\rho_1/\rho_2 \sim 2$. This tends to reduce the growth of short-wavelength perturbations.

A two-dimensional axisymmetric implosion is obtained by perturbing the gas/glass interface at the beginning of the calculation. The perturbed radius is $r = r_0 + a_0 P_4 (\cos \theta)$, where $r_0 = 130 \ \mu$m and $a_0 = 5 \ \mu$m.

The turbulence model calculations use an (r, θ) spherical polar mesh with θ in the range 0 to 90°. The mesh in the radial direction moves with the mean θ-averaged fluid velocity, that is, a semi-Lagrangian calculation is performed. The number of meshes is 160 in the radial direction and 60 in the angular direction (for the asymmetric implosion). Separate temperatures are used for each fluid, and thermal flux terms are included in the internal energy equations. It is therefore necessary to model the thermal flux between fluids. The energy exchange rate per unit volume between fluid r and fluid s is given by:

$$E_{rs} = c_4 \frac{f_r f_s}{L^2} \bar{k}(T_r - T_s),$$

where $\bar{k}$ is an appropriate mean value of k and c_4 is a model constant.

In the calculations shown here, c_4 has been set equal to 20, an appropriate value for a spherical particle of $\frac{1}{2}L$ in a background fluid. It should be possible to obtain a more soundly based value for the model constant from analysis of direct three-dimensional simulations with thermal fluxes included. However, calculation of thermal fluxes is not presently available in TURMOIL3D.

Results are shown here for three calculations. Figure 12 shows the evolution of the long-wavelength RT instability from the P_4 perturbation. In this case interface tracking is used, as described by Youngs (1982), that is, the turbulence model is not activated. At $t = 1.2$ ns, which is 0.25 ns after peak gas compression, the gas bubble is highly asymmetric. Figure 13 shows volume fraction contours at 1.0 and 1.2 ns for the calculations, with and without the P_4 perturbation, using the turbulence model to represent the fine scale mixing at the gas/pusher interface.

Without the P_4 perturbation there is a turbulent mixing zone at the gas/glass interface of thickness about 7 μm at the end of the calculation (1.2 ns). When the P_4 perturbation is included, stretching of the interface leads to a thinner mixing zone, ~4 μm, over much of the surface. There is enhanced mixing where the vortices form behind the spike of glass at 45°.

For the calculation without the P_4 perturbation the mass of glass within the turbulent mixing zone at 1.2 ns is 1.2 μg. This compares with a gas mass of 2.3 μg (for the region $0 < \theta < 90°$). If thermal fluxes are omitted, that is, $k = 0$, the mass of glass in the mixing zone increases to 2.5 μg. Hence, according to the turbulence model, the reduction in Atwood number due to thermal transport has a significant effect. (The mass of glass in the mixing
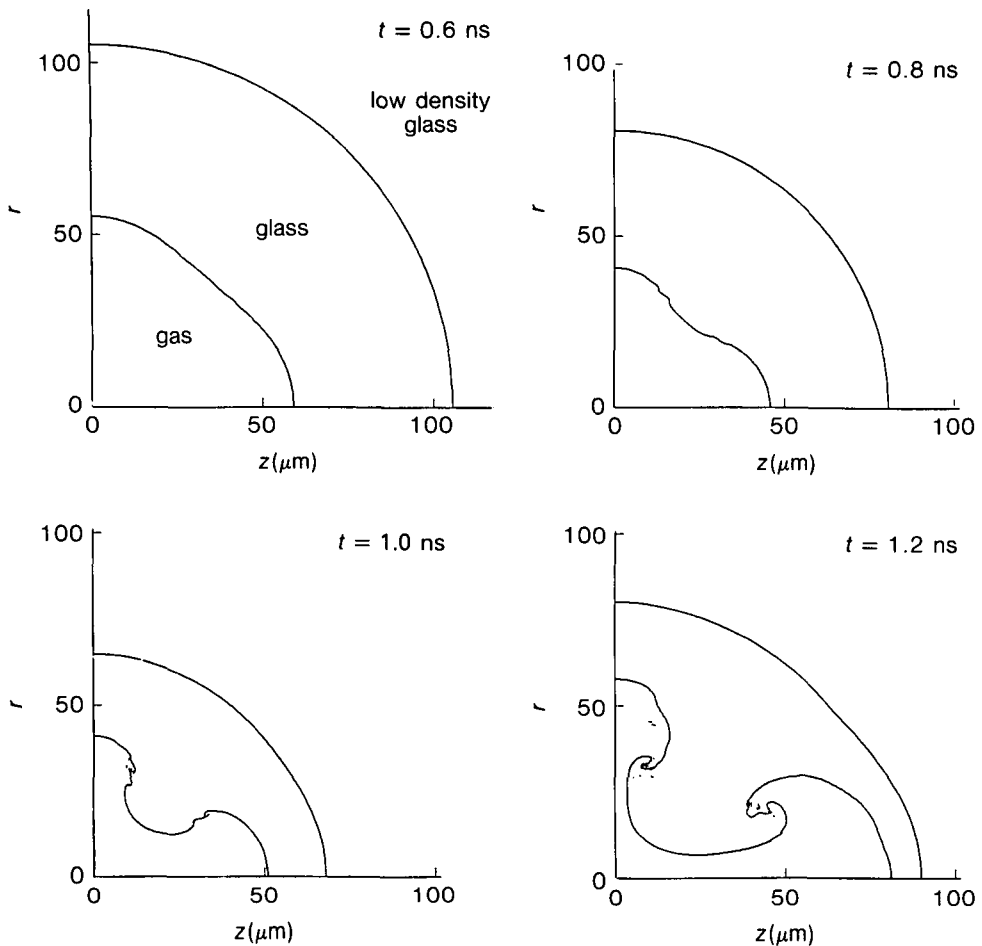
FIGURE 12. Idealized ICF implosion. Two-dimensional simulation with interface tracking.

zone is defined here as the mass of glass in all cells for which the gas mass fraction is greater than 1%.)

8. Conclusions

This paper has given examples of the types of numerical simulations that may be performed on present-day supercomputers to model turbulent mixing at fluid interfaces. Direct three-dimensional simulation has been used to investigate simple RT and RM mixing problems in detail. The importance of performing three-dimensional rather than two-dimensional calculations has been demonstrated. Dissipation of turbulence kinetic energy and density fluctuations by the cascade to high wavenumbers (the Kolmogorov process) is enhanced in three dimensions. For RT mixing the overall growth rate of the mixing zone is similar for two- and three-dimensional simulations. However, there is significantly more mixing at a molecular or atomic level in three dimensions. For the RM case, in which turbulence is generated impulsively, the late time behavior is quite different in the two- and three-
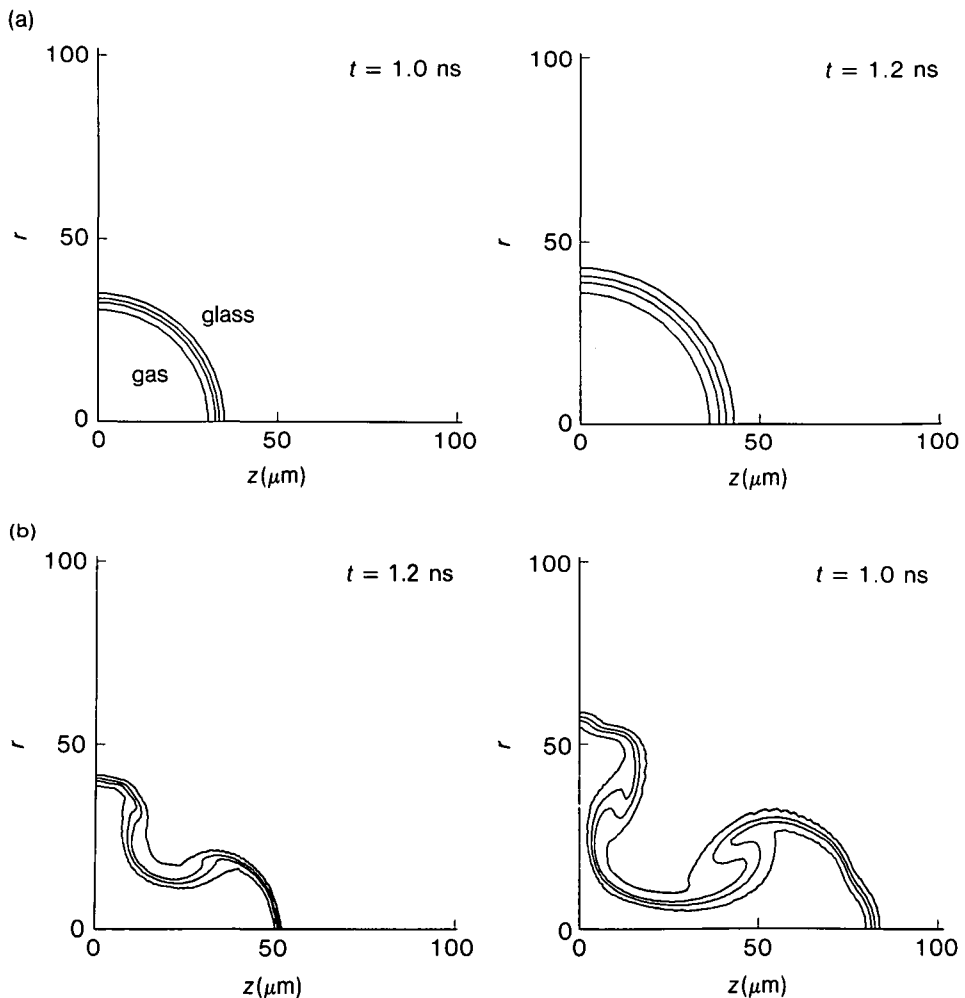
(a)

(b)

FIGURE 13. Idealized ICF implosion. Two-dimensional turbulence model calculations, (a) without P_4 perturbation, (b) with P_4 perturbation.

dimensional simulations. Kinetic energy dissipation in the three-dimensional case leads to significantly slower mixing rates at late time.

It is impractical to apply direct three-dimensional simulation to real problems where many complex physical processes need to be modeled. For this reason a turbulence model is used to represent the average behavior of the turbulent mixing zone in ICF implosions. A two-dimensional turbulence model based on the equations of multiphase flow with turbulent diffusion terms added has been applied to an axisymmetric implosion. A fine computational mesh is needed to resolve the growth of the turbulence accurately. Hence, application of the two-dimensional turbulence model also requires significant computer resources.

Direct three-dimensional simulation can play a very useful role in validation of the two-dimensional turbulence model. It has been shown here that it is possible to make a useful comparison between direct three-dimensional simulation and the two-dimensional turbulence model results for a simple mixing experiment that is two-dimensional on average.

The overall conclusion is that a combination of direct three-dimensional simulation, the application of turbulence models, and experimental validation is capable of providing a detailed understanding of the interfacial mixing processes and an assessment of the effect of turbulent mixing in ICF applications.

Some important aspects of hydrodynamic instabilities in ICF implosions have not been addressed in this paper. Instability growth at the ablation front, where mass ablation has a stabilizing effect, has not been considered here. In some situations there may be a density gradient rather than a sharp interface. This will also reduce instability growth. However, all these phenomena seem to be as amenable to computer modeling as the processes considered here.

REFERENCES

ANDREWS, M.J. 1992 *Advances in Compressible Turbulent Mixing*, W.P. Dannevik, A.C. Buckingham, and C.E. Leith, eds. CONF-8810234, Lawrence Livermore National Laboratory.

ANDREWS, M.J. & SPALDING, D.B. 1990 *Phys. Fluids A* 2,922.

ANDRONOV, V.A. *et al.* 1976 *Sov. Phys. JETP* 44, 424.

ANUCHINA, N.N. *et al.* 1978 *Tr. Izv. Nauk SSSR, Mekh. Zhidk. Gaza* 6, 157.

BARENBLATT, G.I. 1983 *Non-linear Dynamics and Turbulence*, G.I. Barenblatt, G. Loos, and D.D. Joseph, eds. (Pitman, Boston).

BATT, R.G. 1977 *J. Fluid Mech* 82, 53.

BELEN'KII, S.Z. & FRADKIN, E.S. 1965 *Tr. Fiz. Inst. Akad. Nauk SSSR im P N Lebedev* 29, 207.

BESNARD, D.C. & HARLOW, F.H. 1988 *Int. J. Multiphase Flow* 14, 679.

BESNARD, D.C. *et al.* 1989 *Physica* D37, 227.

BROWN, G.L. & ROSHKO, A. 1974 *J. Fluid Mech* 64, 775.

CHERN, I.-L. *et al.* 1986 *J. Comp. Phys.* 62, 83.

CLOUTMAN, L.D. & WEHNER, M.F. 1992 *Phys. Fluids A* 4, 1821.

CROWLEY, W.P. 1992 *Advances in Compressible Turbulent Mixing*, W.P. Dannevik, A.C. Buckingham, and C.E. Leith, eds. CONF-8810234, Lawrence Livermore National Laboratory.

DAHLBURG, J.P. & GARDNER, J.H. 1990 *Phys. Rev. A* 41, 5695.

DALY, B.J. 1967 *Phys. Fluids* 10, 297.

DEBAR, R. 1974 Lawrence Livermore National Laboratory Report UCID-19683.

GARDNER, J.H. *et al.* 1991 *Phys. Fluids* B3, 1070.

GENTRY, R.A. *et al.* 1966 *J. Comp. Phys.* 1, 87.

GLIMM, J. *et al.* 1990 *Phys. Fluids A* 2, 2046.

HARLOW, F.H. & WELCH, J.E. 1966 *Phys. Fluids* 9, 842.

KERR, R.M. 1988 *J. Comp. Phys.* 76, 48.

KUCHERENKO, Yu. A. *et al.* 1991 In *Proc. of Third International Workshop on the Physics of Compressible Turbulent Mixing*, Royaumont, Commissariat à l'Energie Atomique, Paris, France.

LAUNDER, B.E. & SPALDING, D.B. 1972 *Mathematical Models of Turbulence* (Academic Press, London).

MIKAELIAN, K.O. 1991 *Phys. Fluids A* 3, 2638.

MOIN, P. & KIM, J. 1982 *J. Fluid Mech.* 118, 341.

MULDER, W. *et al.* 1992 *J. Comp. Phys.* 100, 209.

NEUVAZHAYEV, V.E. 1975 *Sov. Phys. Dokl.* 20, 398.

NEUVAZHAYEV, V.E. 1991 *Matematicheskoye Modelinovaniye*, 3, 10 (in Russian).

PHAM, T. & MEIRON, D.I. 1993 *Phys. Fluids A* 5, 334.

POLYONOV, A.V. 1991 In *Proc. of Third International Workshop of the Physics of Compressible Turbulent Mixing*, Royaumont, Commissariat à l'Energie Atomique, Paris, France.

READ, K.I. 1984 *Physica* D12, 45.

RICHTMYER, R.D. 1960 *Commum. Pure Appl. Math.* **13**, 297.

SPALDING, D.B. 1987 *Int. J. Multiphase Flow* **24**, 1.

TOWN, R.P.J. & BELL, A.R. 1991 *Phys. Rev. Lett.* **67**, 1863.

TRYGGVASON, G. 1988 *J. Comp. Phys.* **75**, 253.

TRYGGVASON, G. & UNVERDI, S.O. 1990 *Phys. Fluids A* **2**, 656.

VAN LEER, B. 1977 *J. Comp. Phys.* **23**, 276.

YOUNGS, D.L. 1982 *Numerical Methods for Fluid Dynamics*, K.W. Morton and M.J. Baines, eds. (Academic Press, London).

YOUNGS, D.L. 1984 *Physica* **12D**, 32.

YOUNGS, D.L. 1989 *Physica* **D37**, 270.

YOUNGS, D.L. 1991 *Phys. Fluids A* **3**, 1312.